On the Inverse Relationship between the Boreal Wintertime Pacific Jet Strength and Storm-Track Intensity

Yuan-Bing Zhao

School of Atmospheric Sciences, Nanjing University of Information Science and Technology, Nanjing, China

X. San Liang

School of Marine Sciences, and School of Atmospheric Sciences, Nanjing University of Information Science and Technology, Nanjing, China

ABSTRACT

Previous studies show that in boreal winters when the Pacific jet is extremely strong, the Pacific storm track is, however, unexpectedly weak. Using a recently developed technique, namely, the multiscale window transform (MWT), and the MWT-based localized multiscale energetics analysis, we investigate in this study the underlying mechanism of this counterintuitive phenomenon, based on ERA-40 data. It is found that most of the synoptic storms are generated at latitudes far north of the jet core, which lowers the relevance of the jet strength to the storm-track intensity, and the inverse relationship between the Pacific jet strength and storm-track intensity is mainly attributed to the internal dynamics. In the strong jet state, on one hand, the jet is narrow, and thus the jet winds at high latitudes are weak, resulting in weak baroclinic instabilities and hence reduced eddy growth rate; on the other hand, although baroclinic instabilities are strong at the jet core, inverse kinetic energy (KE) cascades are even stronger (by 43%). The resultant effect is that more eddy energy is transferred back to the background flow, leaving an overall weak storm track in a strong Pacific jet. In addition, diabatic processes are found to account for the inverse relationship: it is greatly weakened (by 25%) in the strong-core jet state. Apart from these, we also find that the role that barotropic canonical transfer plays in the inverse relationship is opposite to that in the formation of the midwinter minimum (MWM), another counterintuitive phenomenon in the Pacific storm track.

1. Introduction

The storm track in the atmosphere plays an important role in the midlatitude climate dynamics (e.g., Chang et al. 2002; Swanson 2007). In the Northern Hemisphere (NH), there are two major storm tracks—the Pacific storm track and the Atlantic storm track—which are zonally elongated over the two oceans. According to the linear baroclinic instability theory (Eady 1949; Lindzen and Farrell 1980), the storm track should be strong when the jet is strong. However, Nakamura (1992) found that the Pacific storm track attains its maximum intensity in late fall and early spring, leaving a minimum in midwinter. This phenomenon, which contradicts the linear theory, is called the midwinter minimum (MWM) of the Pacific storm track (see also Christoph et al. 1997; Chang 2003; Deng and Mak 2005). More than this striking seasonal variation, it is further found that there exists an "inverse relation" between the wintertime Pacific

storm-track intensity and the jet-core strength (e.g., Zhang and Held 1999; Chang 2001; Nakamura et al. 2002); in other words, in boreal winter (defined as December–February) when the Pacific jet is strong, the storm-track intensity turns out to be weaker. These two phenomena, which seem to be of the same dynamical origin, actually are different (see the discussion in section 8). In this study, we focus on the "inverse relationship" problem.

During the past decades, many efforts have been made to understand this counterintuitive phenomenon. Based on energy budget diagnostics, Chang (2001) found that, in winters with a strong jet, synoptic waves tend to be trapped in the upper troposphere and have relatively weak low-level circulations. The waves are therefore less efficient to tap available potential energy from the background baroclinicity. Similar observations were made by Nakamura and Sampe (2002) and Harnik and Chang (2004). Besides, Chang (2001) showed that as waves are trapped in upper levels, their group velocity increases because of the strong advection of the upper-level flow. They will pass through

Corresponding author: X. San Liang, x.san.liang@gmail.com

the strong baroclinic zone more quickly, and the eddy spatial growth rate is therefore reduced. But later on, Nakamura et al. (2002) and Harnik and Chang (2004) found that the increase in group velocity in a strong jet can only explain a small part of the suppression in eddy growth rate, since as the jet strengthens, the increase in maximum growth rate is strong enough to counteract the effect of the increased group velocity.

Besides jet strength, the inverse relationship may be related to jet width. Harnik and Chang (2004) found that in boreal winter, a stronger Pacific jet tends to be narrower, and the narrowing of a jet may inhibit its eddy growth rate by decreasing the meridional wavelength of the baroclinic waves. But this argument is based on the assumption that the meridional scale of storms is determined by the jet width (Ioannou and Lindzen 1986), which has little evidence support so far (Penny et al. 2010).

Recently, Penny et al. (2013) argued that the linear baroclinic instability theory actually still holds over the Pacific despite the overall inverse relationship. They found that regions with stronger (weaker) zonal wind have stronger (weaker) storminess, and the overall decrease in storminess over the Pacific is most linked to the weaker amplitude of individual storms in strong jet months. But why these individual storms are weaker is still an issue.

In this study, we apply a newly developed functional analysis technique, namely, the multiscale window transform (MWT; Liang and Anderson 2007), and the MWT-based localized multiscale energy and vorticity analysis (MS-EVA; Liang and Robinson 2005, 2007; Liang 2016) to reinvestigate the inverse-relation problem. Multiscale energetics analysis can provide quantitative information of intrinsic and external energy sources and sinks and has proved to be a powerful approach to storm-track dynamical studies (e.g., Chang and Orlanski 1993; Cai et al. 2007; Mak and Deng 2007; Lee et al. 2011). In traditional energetics diagnostics, a field is decomposed into two parts, namely, a time-mean part and a perturbation part. Such a decomposition, however, cannot distinguish the low-frequency variations from the synoptic-scale perturbations, and thus the resulting eddy energetics are "polluted" by the low-frequency variabilities. For time-varying energetics, even the very basic problem, that is, how perturbation energy is represented in such a framework, is yet to be fixed. Besides, the most important part that accounts for nonlinear interactions in a flow, that is, the energy transfer between the two different scales, has been found to be ambiguous in the classical formalism (e.g., Plumb 1983). These problems, among others, are to be resolved in a unified treatment in MS-EVA.

It should be noted that, although the inverse-relationship problem has been examined before from the perspective of energetics (e.g., Chang 2001; Deng and Mak 2006), this work is by no means a repetition of previous studies. As we will see soon in the next section, the method used for this study is quite different from the traditional methods, especially in its decomposition of the background and synoptic fields and in the rigorous formulation of the interaction process between them, which accounts for most of the differences between this and previous studies. Besides, in the traditional energetics studies in this regard, usually spatial averages, for example, the meridional average (Chang 2001), are used, while the energetics processes in the North Pacific have significant regional characteristics (Chang et al. 2002; Deng and Mak 2006; Cai et al. 2007; Lee et al. 2011) or are even rich in spatial structure (e.g., Penny et al. 2013). Obviously, averaging over space prohibits us from a grasp of this spatial structure. Moreover, previous studies mostly focus on the western Pacific (e.g., Chang 2001; Harnik and Chang 2004). But the main body of the North Pacific storm track is actually located in the central and eastern Pacific (Blackmon et al. 1977; Chang et al. 2002; Chang 2003), and the inverse-relationship phenomenon is significant in the entire North Pacific storm-track area (e.g., Chang 2001; Penny et al. 2013). Considering these issues, among others, there is still a gap between our understanding and the real energetics processes underlying the phenomenon. This study aims to fill the gap.

The rest of this paper is organized as follows. In section 2, we briefly introduce MWT and MS-EVA. Section 3 is a description of the data. The application begins in section 4, where the MS-EVA is set up. In section 5, we show how the two states (strong and weak) of the Pacific winter jet are obtained. Then the storm-track energetics of the two jet states are analyzed (section 6) and discussed (section 7). This study is summarized in section 8.

2. Methods

a. MWT and MS-EVA

The research methodology for this study is the MS-EVA by Liang and Robinson (2005). A recently updated comprehensive introduction is seen in Liang (2016). Also to be used is the MS-EVA-based theory of localized finite-amplitude baroclinic and barotropic instabilities (Liang and Robinson 2007). This is a systematic line of work involving components from different disciplines such as functional analysis and geophysical fluid dynamics. A detailed description of MS-EVA is beyond the scope of this paper; in this section, we only present a very brief introduction. For details and comparison with traditional local and global energetics formalisms, refer to Liang (2016) and the references therein.

MS-EVA is based on a new functional analysis tool called MWT developed by Liang and Anderson (2007).

Using MWT, one can decompose a function space into a direct sum of several mutually orthogonal subspaces, each with an exclusive range of time scales, while preserving its time–locality properties. We will call such a subspace a scale window or simply a window. One may have as many windows as they wish; for this study, we select two, namely, a low-frequency basic-flow window (or background flow window) and a synoptic-scale window (or transient window). For easy reference, they are denoted and will be referred to as windows $\varpi = 0$ and 1, respectively.

Given a time series $T(t)$ with N steps, application of MWT yields two types of quantities: one is the MWT transform coefficients $\hat{T}_n^{\sim\varpi}$ ($n = 1, 2, \ldots, N$, corresponding to the time location in t), another the multiscale window reconstruction (MWR) $T^{\sim\varpi}(t)$ for $\varpi = 0$ and 1. The reconstructions $T^{\sim\varpi}(t)$ are just like the low- and high-pass-filtered quantities. For example, in a two-window decomposition in this study, the series $T(t)$ is decomposed into

$$T = T^{\sim 0} + T^{\sim 1}, \tag{1}$$

where $T^{\sim 0}$ stands for the background field and $T^{\sim 1}$ the transient field. MWT and MWR form a transform pair, but they are distinctly different concepts, with the former defined in phase space, while the latter in physical space. The MWR of $T(t)$ on the synoptic-scale window, for example, corresponds to a high-pass filtered signal. But the MWT of $T(t)$ is conceptually different. The MWT has many nice properties, one being the property of marginalization, which allows for a precise representation of multiscale energy as the product of the MWT coefficients (up to some constant). For example, the transient eddy energy extracted from $T(t)$ is simply $(\hat{T}_n^{\sim 1})^2$ multiplied by some constant. (Note one cannot write it in terms of the filtered quantities such as $(T^{\sim 1})^2$! This is a conceptual error that, unfortunately, has frequently appeared in the literature. This is the very difficulty with the classical filters that

cannot have energy represented.) Since $\hat{T}_n^{\sim 1}$ is localized, with location labeled by n, this essentially solves the oddity between localization and multiscale decomposition.

One may argue that orthonormal wavelet transforms (the concept of energy can only be introduced with orthogonal transforms) can be equally utilized to fulfill the goal of this study. In this case, we are studying storms (or eddies), which are defined on a range of scales, or scale windows as introduced above, rather than individual scales. To represent the energy of a storm, we must summarize the energies over the scale levels within the window. However, for an orthonormal wavelet transform, the transform coefficients for different scale levels are discretely defined at different locations, making the summation impossible. In contrast, MWT is a transform with respect to some subspace or scale window as it is called, rather than individual scales. In principle it does not rely on the basis, though in practice a basis, such as the orthonormalized cubic spline basis in Liang and Anderson (2007), is used for illustration and computation.

With MWT, the available potential energy (APE) and kinetic energy (KE) densities on window ϖ at location n can be defined, following Lorenz (1955), as

$$A_n^\varpi = \frac{1}{2} c (\hat{T}_n^{\sim\varpi})^2 \quad \text{and} \tag{2}$$

$$K_n^\varpi = \frac{1}{2} \hat{\mathbf{v}}_{h,n}^{\sim\varpi} \cdot \hat{\mathbf{v}}_{h,n}^{\sim\varpi}. \tag{3}$$

In the above definitions, $\mathbf{v}_h = (u, v)$ is the horizontal velocity, T is the temperature anomaly [with the mean vertical profile $\overline{T}(z)$ removed], and $c = g/[\overline{T}(g/c_p + \overline{T}_z)]$ (c_p is the specific heat capacity of air for isobaric processes) is a proportionality depending on the buoyancy frequency. The multiscale energy equations for Earth atmosphere, with location n in the subscript omitted henceforth for clarity, are

$$\frac{\partial A^\varpi}{\partial t} = \underbrace{-\nabla \cdot \left[\frac{1}{2} c \widehat{(\mathbf{v}T)}^{\sim\varpi} \hat{T}^{\sim\varpi} \right]}_{\Delta Q_A^\varpi} + \underbrace{\frac{1}{2} c [\widehat{(\mathbf{v}T)}^{\sim\varpi} \cdot \nabla \hat{T}^{\sim\varpi} - \hat{T}^{\sim\varpi} \nabla \cdot \widehat{(\mathbf{v}T)}^{\sim\varpi}]}_{\Gamma_A^\varpi} + \underbrace{\hat{\omega}^{\sim\varpi} \hat{\alpha}^{\sim\varpi}}_{-b^\varpi}$$
$$+ \underbrace{\frac{1}{2} \hat{T}^{\sim\varpi} \widehat{(\omega T)}^{\sim\varpi} \frac{\partial c}{\partial p} + \frac{1}{\overline{T}} \hat{T}^{\sim\varpi} \widehat{(\omega \alpha)}^{\sim\varpi}}_{S_A^\varpi} + F_A^\varpi \quad \text{and} \tag{4}$$

$$\frac{\partial K^\varpi}{\partial t} = \underbrace{-\nabla \cdot (\hat{\mathbf{v}}_h^{\sim\varpi} \hat{\Phi}^{\sim\varpi})}_{\Delta Q_P^\varpi} + \underbrace{\frac{1}{2} \{ \widehat{(\mathbf{v}\mathbf{v}_h)}^{\sim\varpi} : \nabla \hat{\mathbf{v}}_h^{\sim\varpi} - [\nabla \cdot \widehat{(\mathbf{v}\mathbf{v}_h)}^{\sim\varpi}] \cdot \hat{\mathbf{v}}_h^{\sim\varpi} \}}_{\Gamma_K^\varpi} + \underbrace{\left(-\nabla \cdot \left[\frac{1}{2} \widehat{(\mathbf{v}\mathbf{v}_h)}^{\sim\varpi} \cdot \hat{\mathbf{v}}_h^{\sim\varpi} \right] \right)}_{\Delta Q_K^\varpi}$$
$$+ \underbrace{(-\hat{\omega}^{\sim\varpi} \hat{\alpha}^{\sim\varpi})}_{b^\varpi} + F_K^\varpi, \tag{5}$$

for windows $\varpi = 0$ and 1. In (4) and (5) $\mathbf{v} = (u, v, \omega)$ is the three-dimensional velocity, and the other symbols are conventional. The colon operator (:) in (5) is defined such that, for two dyadic products $\mathbf{AB}$ and $\mathbf{CD}$, $(\mathbf{AB})$: $(\mathbf{CD}) = (\mathbf{A} \cdot \mathbf{C})(\mathbf{B} \cdot \mathbf{D})$.

One can see that, within the MWT framework, the KE and APE equations for the two different windows have the same form (compared to the traditional mean and eddy energetics equations in the Lorenz formalism). The naming convention for these terms in (4) and (5) is the same as others (e.g., Orlanski and Katzfey 1991; Chang 1993; Yin 2002), but, as we will see soon, some of them have distinctly different expressions. In (4), the term on the left-hand side is the time tendency of APE. The first term on the right ΔQ_A^ϖ is the convergence (note the minus sign) of the APE flux. The second term Γ_A^ϖ is the transfer of APE to the designated scale window ϖ from the other windows. (Note the expressions of these two terms are completely different from the corresponding traditional ones; see below.) The third term b^ϖ represents buoyancy conversion between APE and KE on the designated scale window, and it is defined as positive if the conversion is from APE to KE. The sum of the fourth and fifth terms S_A^ϖ is due to the vertical variation of statistic stability c; it is usually small. The last term F_A^ϖ denotes the residue of the APE equation; it mainly accounts for the APE generation (or dissipation) through diabatic processes. In (5), the term on the left-hand side is the time tendency of KE. The first term on the right-hand side ΔQ_P^ϖ is the geopotential flux convergence or pressure work, the second term Γ_K^ϖ the transfer of KE to scale window ϖ from the other windows, the third term ΔQ_K^ϖ the KE flux convergence, and the fourth the buoyancy conversion, which is the same as that in (4) but with an opposite sign. The last term F_K^ϖ denotes the frictional dissipation. Note that all the terms are localized both in space and in time; in other words, they are all four-dimensional field variables, distinguished notably from the classical formalisms in which localization is lost in at least one dimension of space–time in order to achieve scale decomposition. Processes intermittent in space and time are thus naturally embedded in (4) and (5). A schematic of the flowchart is shown in Fig. 1.

Although the terms in (4) and (5) have the conventional names, they are actually distinctly different from those in the traditional formalisms. The most distinct terms are Γ_A^ϖ and Γ_K^ϖ, which are the processes that we are most interested in for this study. For a scalar field T in a flow $\mathbf{v}$, the energy transfer from other scale windows to window ϖ proves [see Liang (2016) for a rigorous proof]
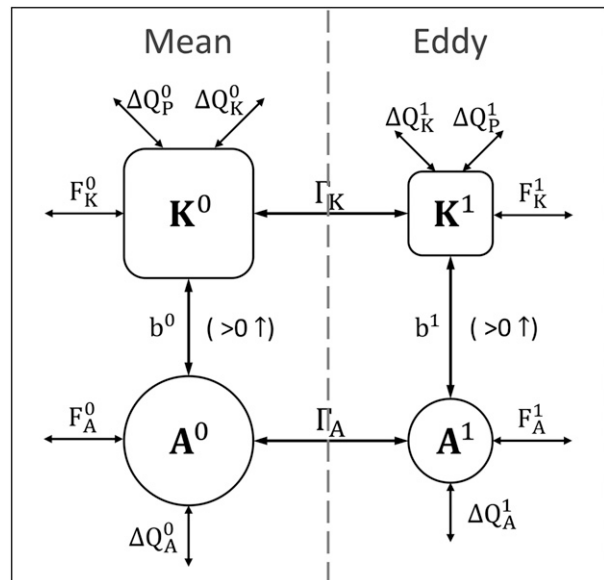

FIG. 1. A schematic of the multiscale energy pathway for a two-window decomposition. Refer to (4) and (5) for an explanation of the symbols.

$$\Gamma^\varpi = -E^\varpi \nabla \cdot \mathbf{v}_T^\varpi = \frac{1}{2}[\widehat{(\mathbf{v}T)}^{\sim\varpi} \cdot \nabla \hat{T}^{\sim\varpi} - \hat{T}^{\sim\varpi} \nabla \cdot \widehat{(\mathbf{v}T)}^{\sim\varpi}],$$

(6)

where $E^\varpi = (1/2)(\hat{T}^{\sim\varpi})^2$ is the energy on window ϖ. (When needed, a constant should be multiplied on both sides. For example, if T is temperature, then E^ϖ and Γ^ϖ should be both multiplied by c to make APE and baroclinic energy transfer.) The other symbol,

$$\mathbf{v}_T^\varpi = \frac{\widehat{(\mathbf{v}T)}^{\sim\varpi}}{\hat{T}^{\sim\varpi}},$$

(7)

is referred to as the T-coupled velocity. As proved in Liang (2016), the right-hand side of (6) has a Lie bracket form; it possesses the property of Jacobian identity, reminiscent of the Poisson bracket in Hamiltonian dynamics. With (7), the barotropic energy transfer in (5) can be written as

$$\Gamma_K^\varpi = -\frac{1}{2}[(\hat{u}^{\sim\varpi})^2 \nabla \cdot \mathbf{v}_u^\varpi + (\hat{v}^{\sim\varpi})^2 \nabla \cdot \mathbf{v}_v^\varpi].$$

(8)

The term Γ^ϖ possesses a very interesting property, namely,

$$\sum_\varpi \sum_n \Gamma_n^\varpi = 0,$$

(9)

as first proposed in Liang and Robinson (2005) and later proved in Liang (2016). Physically, this implies that the transfer is a mere redistribution of energy among the

scale windows, without generating or destroying energy as a whole. This property, though simple to state, does not hold in previous energetics formalisms [refer to Liang and Robinson (2007) for a clear comparison to the classical formalism; in particular, compare the traditional two-scale energy equations, (4) and (5), to the equations resulting from MS-EVA, (19) and (20)]. To distinguish it from those that may have been encountered in the literature, the above transfer is termed canonical transfer; correspondingly the baroclinic and barotropic transfers are called baroclinic and barotropic canonical transfers, respectively.

It has been established that the canonical transfer terms Γ_A^ϖ and Γ_K^ϖ in (4) and (5) are very important. Particularly, the mean-to-eddy parts of them (written as $\Gamma_A^{0\to1}$ and $\Gamma_K^{0\to1}$) correspond precisely to the two important geophysical fluid flow processes, that is, baroclinic instability and barotropic instability [see Liang and Robinson (2007) for a rigorous proof]. For more details, refer to the recent publication Liang (2016).

b. Lagrangian statistical method

Also used in this study is the feature-tracking technique by Hodges (1995). It first identifies the synoptic systems, then tracks them and records the information of their intensities and geographical locations at each step. In practice, the maxima of the relative vorticity ξ at the pressure level (e.g., 850 hPa) are chosen as the indicator of the storm center (or feature point), which forms the nodes of the storm trajectory (Hoskins and Hodges 2002). Following previous studies, the starting time (or genesis time) is defined as the first time when ξ exceeds $1 \times 10^{-5}\,\mathrm{s}^{-1}$. In this study, we only analyze the storms whose ξ remains larger than $1 \times 10^{-5}\,\mathrm{s}^{-1}$ for at least 2 days after their genesis and that propagate more than 1000 km during their lifetime. To reduce the impact of the background flow on the tracking processes, the relative vorticity ξ is first filtered so that only synoptic-scale signals are retained. In the present study, we use the synoptic fields reconstructed by the MWT (see section 4) to fulfill this purpose.

Based on the feature-track dataset, we next compute the statistics through a simple grid box counting and averaging. Two major statistics are computed, including the track density and storm intensity. We first divide the study region (i.e., the Pacific storm track in this study) into latitude–longitude grids, each with a side length of 5°. That is to say, each grid is equivalent to a 5° spherical cap. Second, if a storm enters or passes through a grid, the track density of that grid increases by 1. The raw density statistics are subsequently scaled to number densities per month (30 days) for analysis and display. The storm intensity of one grid is simply defined as the mean strength of the relative vorticity of all the feature points once within it.

3. Data

We use for our study the 40-yr European Centre for Medium-Range Weather Forecasts (ECMWF) Re-Analysis (ERA-40) dataset (Uppala et al. 2005), which has been widely used in storm-track research (e.g., Chang and Guo 2007; Penny et al. 2010). It has a spatial resolution of 2.5° × 2.5° with 23 levels from 1000 to 1 hPa and a temporal resolution of 6 h from September 1957 to July 2002. Details can be found on the ECMWF website (http://apps.ecmwf.int/datasets/data/era40-daily/levtype=pl). Hereafter we will need the fields of velocity components u, v, and ω; geopotential ϕ; and temperature T.

4. MS-EVA setup

The analysis begins with a determination of the scale window bounds. In this study, we need two windows: a synoptic-scale window and a low-frequency background-flow window. According to previous studies, these windows bounded by a period of 16 days (in MWT the number of time steps is required to be a power of 2). This is essentially the same as Deng and Mak (2006), who applied a 15-day high-pass filter in their diagnostics. Besides, Anderson et al. (2003) stated that bandpass filtering with a time period of 2.5–6 days (e.g., Blackmon 1976) may have a detrimental impact on individual weather systems (see also Chang 1993), and a 20-day high-pass filter is a good choice. (We have also tried 8 days as the window bound and found that the results are essentially the same.)

5. Two states of the wintertime Pacific jet

MS-EVA is capable of providing the four-dimensional (4D) spatiotemporal structures for the multiscale energetics. In this study, the composite analysis method is used to analyze the MS-EVA output. We first select the strong and weak wintertime (December–February) jets, and, respectively, average over the selected subsets; the averages are then used to represent the strong and weak jet states. Following previous studies (Chang 2001; Harnik and Chang 2004; Penny et al. 2013), we first define a monthly wind index that can represent the jet strength. It is calculated as the monthly zonal wind speed averaged within the Pacific jet core area (20°–50°N, 120°–170°E) at the 300-hPa level. Then, we pick 20 months with the largest wind index and 20 months with the smallest wind index out of the 135 winter months. Following
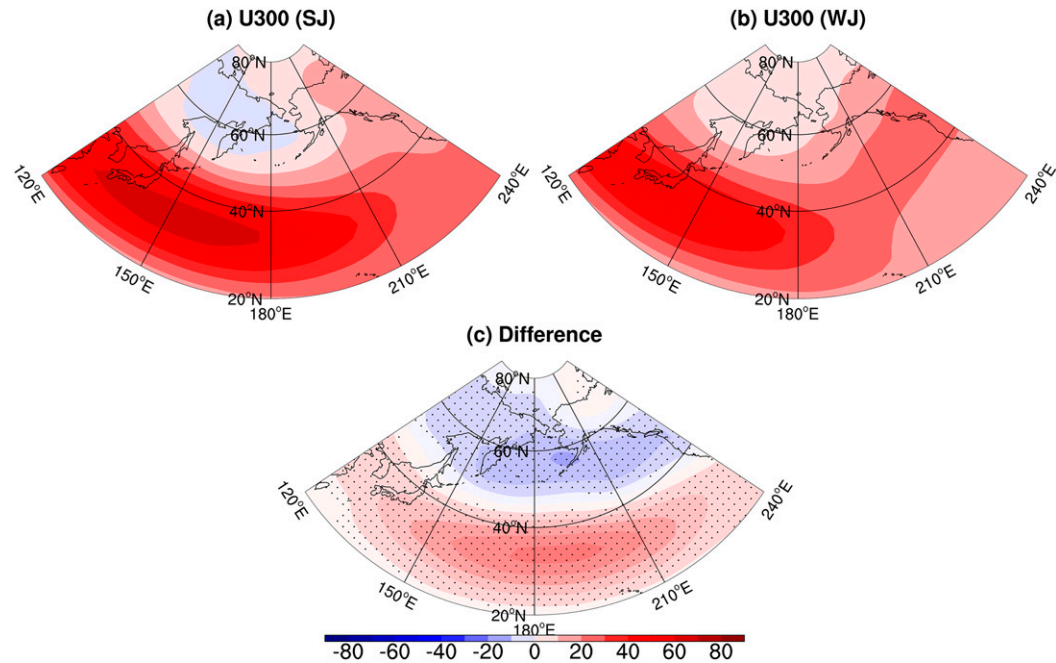
FIG. 2. Distributions of the composite 300-hPa zonal wind $(\mathrm{m\,s^{-1}})$ (a) averaged over 20 SJ months and (b) averaged over 20 WJ months. (c) The difference between (a) and (b). Here and in subsequent figures, except Fig. 6, the stippled regions are significant at the 0.05 level using the two-sided t test.

Penny et al. (2013), hereafter we call them the strong-core jet (SJ) months and the weak-core jet (WJ) months, respectively. Note that in some previous studies of the inverse relationship only the midwinter months (January and February) are considered (e.g., Chang 2001; Nakamura et al. 2002), whereas in some others (e.g., Penny et al. 2013) all winter months are included. We have tried both and the results are essentially the same.

The composite maps of the 300-hPa zonal winds on the basic-flow window are shown in Fig. 2 (almost the same as that of the total field). We see that over the northwest Pacific sector, the strong-core jet (Fig. 2a) is much stronger and more zonally elongated than the weak-core jet (Fig. 2b), which tilts slightly from southwest to northeast. However, the strong-core jet width, measured by the distance between the latitudes at which the winds reach their half peak value, is about 15% meridionally narrower than the weak-core jet. Both jets are located at about 32.5°N, with no obvious meridional shift in the jet-core latitude at the jet entrance region. The difference in the zonal wind between the two jet states shows a dipole pattern, with positive and negative anomalies south and north of 45°N, respectively (Fig. 2c). The anomalies can be as large as 20 and $-15\,\mathrm{m\,s^{-1}}$ in the south and north. The difference is statistically significant by a two-sided t test (Wilks 2011), in agreement with Penny et al. (2013). In the following,

the inverse relationship is examined through differentiating these two states.

6. Energetics of the Pacific storm track

a. Transient eddy energy

We first look at the transient eddy energy. Figure 3 shows the maps of vertically integrated transient available potential energy (TAPE) and transient kinetic energy (TKE) between 1000 and 100 hPa. It can be seen that the main part of the Pacific storm track represented by the transient eddy energy is located downstream and on the north flank of the jet. The difference between the two-state TAPEs shows a dipole pattern, with a negative band over the mid- to high latitudes and a positive band to the south (Fig. 3c), corresponding well to that of Fig. 2c. That is to say, the area with positive (negative) jet wind anomaly has positive (negative) TAPE anomaly. Besides, the negative TAPE anomaly in the north is stronger than the positive anomaly in the south. On the whole, the TAPE in the strong-core jet case is 8.3% less than that in the weak-core jet case (the percentage here is calculated as the difference of the TAPEs between the two jet states divided by the weak jet TAPE; same below).

For TKE, it is also stronger in the weak-core jet months than in the strong-core jet months over almost the whole North Pacific (especially at high latitudes),
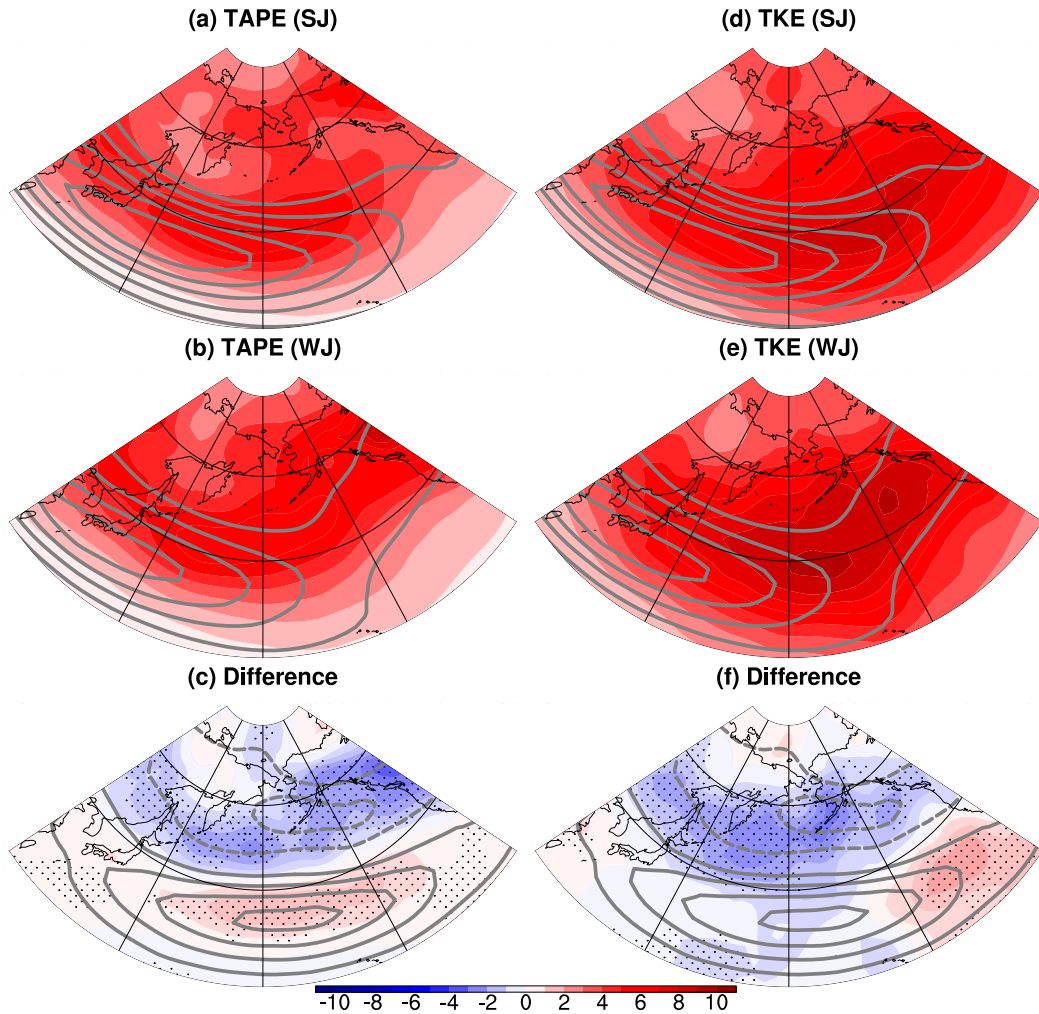
FIG. 3. Horizontal distributions of the vertically integrated transient eddy energy ($10^5 \, \text{m}^2 \, \text{s}^{-2}$) for (a) TAPE for the strong-core state and (b) TAPE for the weak-core state. (c) The difference between (a) and (b). (d)–(f) As in (a)–(c), respectively, but for TKE. The gray contours denote the zonal wind as shown in Fig. 2.

except in the southeast corner (Fig. 3f). This is because in the weak-core state, the basic flow over the eastern Pacific steers to high latitudes, leaving an area of weak zonal wind in the southeast corner (Fig. 3e). The zonal wind is so weak over there that the Rossby wave propagation could be inhibited (Randel and Held 1991; Lorenz 2014). On the whole, the TKE is 10.3% less in the strong-core jet case than in the weak-core jet case. In a word, both TAPE and TKE are generally suppressed in the strong-core jet months.

b. Eddy–basic flow interaction

Figures 4a–4c show the maps of vertically integrated baroclinic transfer from the background flow to the transients $\Gamma_A^{0\to1}$. We see that in both jet states, $\Gamma_A^{0\to1}$ is positive over the entire North Pacific (Figs. 4a,b). The maximum transfers happen to the east coast of Asia,

lying in parallel to the jets but northward of the jet core by about 10 latitudes. As we elucidated previously, positive values of $\Gamma_A^{0\to1}$ indicate baroclinic instability of the background flow and downscale transfer of APE to the transients. The difference in $\Gamma_A^{0\to1}$ between the two jet states shows a dipolar structure similar to that in Fig. 3c. In places where the jet wind is strong (weak), $\Gamma_A^{0\to1}$ is strong (weak), just as one may expect from the linear baroclinic instability theory (e.g., Eady 1949; Lindzen and Farrell 1980; Penny et al. 2013): baroclinic eddy growth rate is proportional to jet wind speed. Also displayed in the figure (Figs. 4d–f) is buoyancy conversion b^1 on the eddy window. Clearly, it has a distribution similar to $\Gamma_A^{0\to1}$, implying that, for the strong-core case, there is less (more) energy conversion from TAPE to TKE in the north (south) of the jet core.
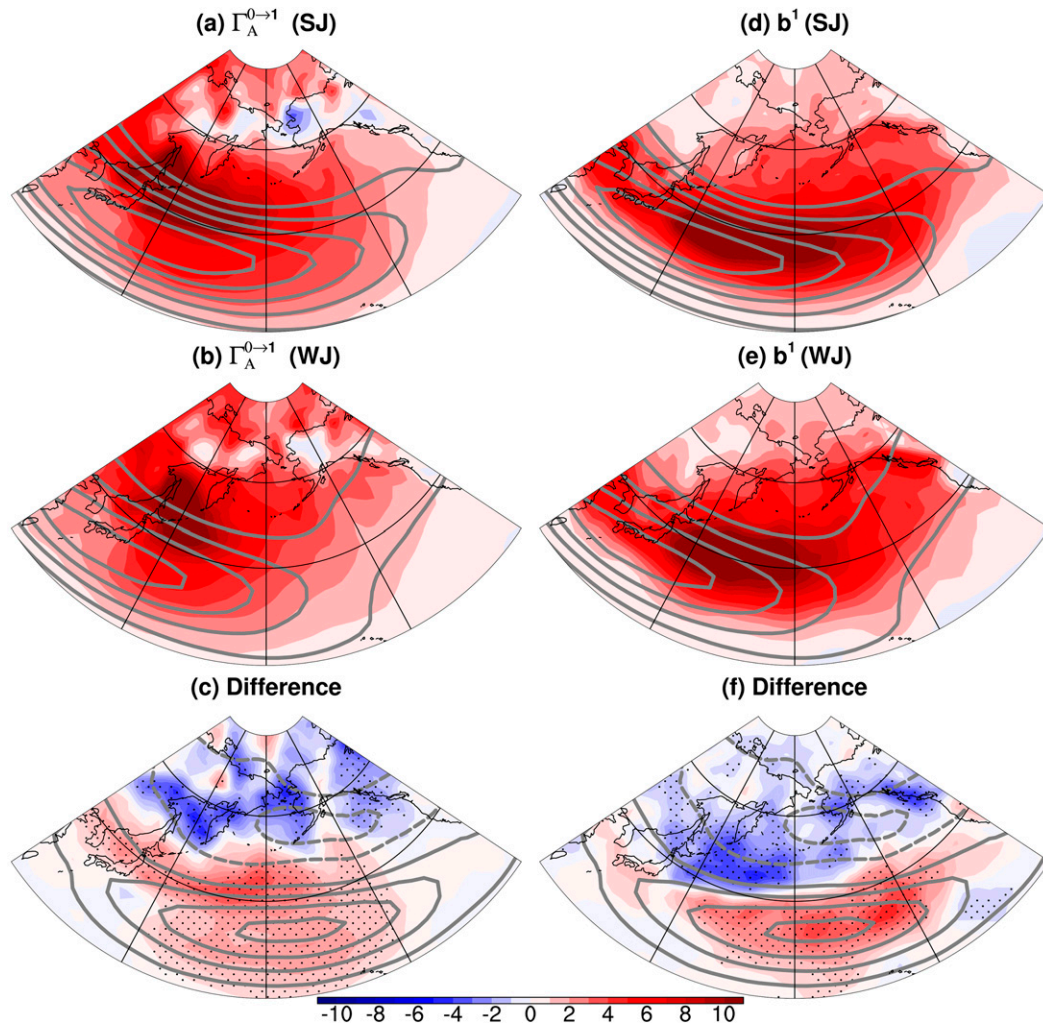
FIG. 4. Horizontal distributions of the vertically integrated baroclinic canonical transfer ($m^2 s^{-3}$) for the (a) strong-core state and (b) weak-core state. (c) The difference between (a) and (b). (d)–(f) As in (a)–(c), respectively, but for buoyancy conversion.

The barotropic transfer $\Gamma_K^{0 \to 1}$ has a different distribution. As shown in Fig. 5, it is positive at the jet core for both states, indicating downscale KE transfer from the background flow to synoptic eddies. Both on the northern flank of the positive center and over the central and eastern Pacific, $\Gamma_K^{0 \to 1}$ is negative; that is to say, over there KE is transferred back to the background flow. The negative $\Gamma_K^{0 \to 1}$ center generally coincides with that of TKE (Figs. 3d,e). For the strong-core jet case, the upscale KE transfer increases with longitude, maximized over the eastern Pacific. This is in contrast to the weak-core case, in which the transfer maximum occurs over the central Pacific. Figure 5c shows the difference in $\Gamma_K^{0 \to 1}$ between the two states. The most remarkable feature is the negative center over the eastern Pacific; in other words, more TKE is transferred back to the

background flow for strong-core jets, which leads to quicker decay of the individual storms in this case. This makes sense, as found in the theoretical study by James (1987) and Deng and Mak (2005) that the strong horizontal shear associated with a strong and narrow jet may lead to strong upscale KE transfer. A dynamical implication is that eddies over the Pacific provide feedback to partially maintain the preexisting anomalous jet state (e.g., Chang and Guo 2007; Penny et al. 2013).

Compared to the absolute values of the barotropic (BT) and baroclinic (BC) energy transfers, their relative values (i.e., $\Gamma_A^{0 \to 1}$/TAPE and $\Gamma_K^{0 \to 1}$/TKE) can better reflect the efficiency of eddies to tap (return) energy from (to) the background flow, and hence are more relevant to the discussion of the structure of eddies and

(a) $\Gamma_K^{0\to1}$ (SJ) (b) $\Gamma_K^{0\to1}$ (WJ)

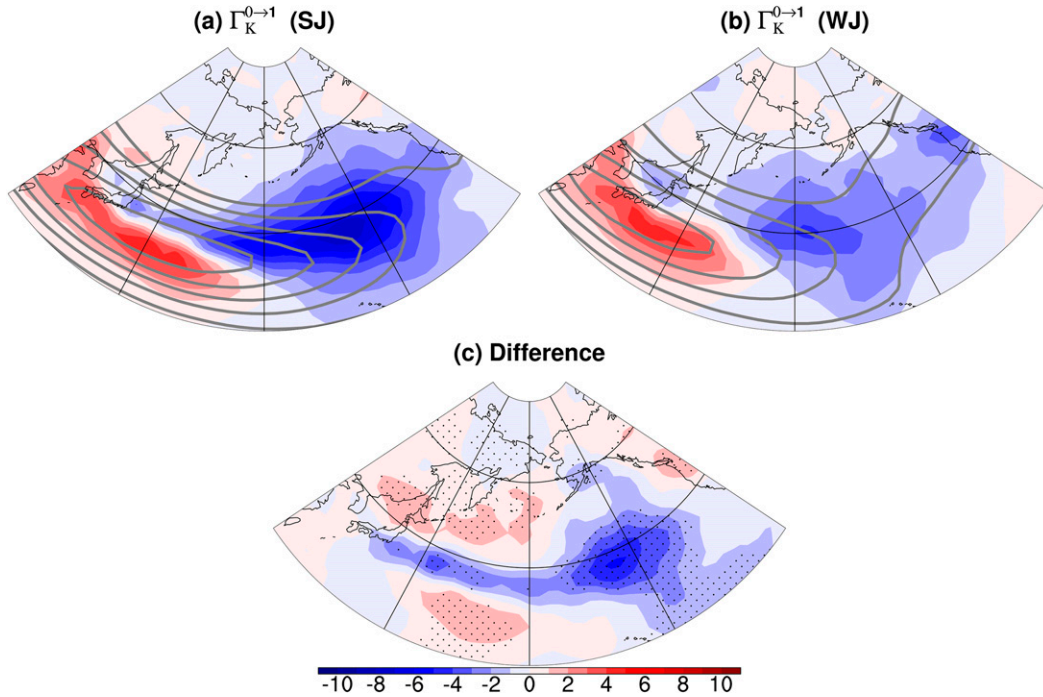(c) Difference

-10 -8 -6 -4 -2 0 2 4 6 8 10

FIG. 5. As in Fig. 4, but for barotropic canonical transfer.

the mechanism in suppressing baroclinic wave intensity (Chang 2001; Deng and Mak 2006). For this purpose, let

$$BC = \frac{\Gamma_A^{0\to1}}{TAPE} \quad \text{and} \quad BT = \frac{\Gamma_K^{0\to1}}{TKE} \qquad (10)$$

[an extra factor of 1/2 may be more relevant; refer to Chang (2001) and Deng and Mak (2006)]. Based on the calculations (Table 1), there is a significant difference between the energy transfers (i.e., $\Gamma_A^{0\to1}$ and $\Gamma_K^{0\to1}$) and their efficiencies (i.e., BC and BT), especially for the baroclinic transfer. If the Pacific storm track is taken as a whole, the difference in $\Gamma_A^{0\to1}$ between the strong and the weak jet states is not significant ($0.11 \times 10^{14}\,J\,s^{-1}$), but the difference in BC is significant ($0.13 \times 10^{-5}\,s^{-1}$),

quite different from the conclusion before (e.g., Nakamura 1992; Chang 2001; Harnik and Chang 2004). Previous studies suggest that changes in storm structure in the strong jet may result in a decrease in baroclinic growth rate, whereas the results here imply that, though the storm structure in the jet center may change in the strong jet state, the change favors a stronger baroclinic growth rate rather than a weaker one.

We further divide the Pacific storm track into two regions, that is, the southern region and the northern region, along 45°N, and then discuss $\Gamma_A^{0\to1}$ and BC in each region (cf. Table 1). In the southern region, $\Gamma_A^{0\to1}$ and BC are consistent with each other. Both of them are stronger in the strong jet case ($1.0 \times 10^{14}\,J\,s^{-1}$ and $1.0 \times 10^{-5}\,s^{-1}$) than in the weak case ($0.71 \times 10^{14}\,J\,s^{-1}$

TABLE 1. Energies and energy transfers integrated over the Pacific storm-track regions for the two jet states for entire domain (20°–70°N, 120°–240°E), western domain (20°–70°N, 120°E–180°), eastern domain (20°–70°N, 180°–240°E), southern domain (20°–45°N, 120°–240°E), and northern domain (45°–70°N, 120°–240°E). A value in boldface means that the difference in that quantity between the two jet states (SJ and WJ) is significant at the 0.05 level using the two-sided t test.

|	Entire (120°–240°E)		Western (120°E–180°)		Eastern (180°–240°E)		Southern (20°–45°N)		Northern (45°–70°N)	
Jet type	SJ	WJ	SJ	WJ	SJ	WJ	SJ	WJ	SJ	WJ
TAPE (10^{19} J)	1.79	1.95	0.92	0.99	0.99	1.09	1.00	0.93	**0.78**	**1.01**
TKE (10^{19} J)	2.55	2.85	**1.10**	**1.29**	1.60	1.70	1.65	1.69	**0.91**	**1.16**
$\Gamma_A^{0\to1}$ (10^{14} J s^{-1})	1.54	1.43	1.13	1.09	0.49	0.45	**1.00**	**0.71**	**0.53**	**0.71**
$\Gamma_K^{0\to1}$ (10^{14} J s^{-1})	**−0.46**	**−0.32**	0.09	0.04	**−0.56**	**−0.37**	**−0.32**	**−0.12**	−0.14	−0.20
BC (10^{-5} s^{-1})	**0.86**	**0.73**	**1.23**	**1.10**	0.49	0.41	**1.00**	**0.77**	0.68	0.70
BT (10^{-5} s^{-1})	**−0.18**	**−0.11**	0.08	0.03	**−0.35**	**−0.22**	**−0.19**	**−0.07**	−0.15	−0.17
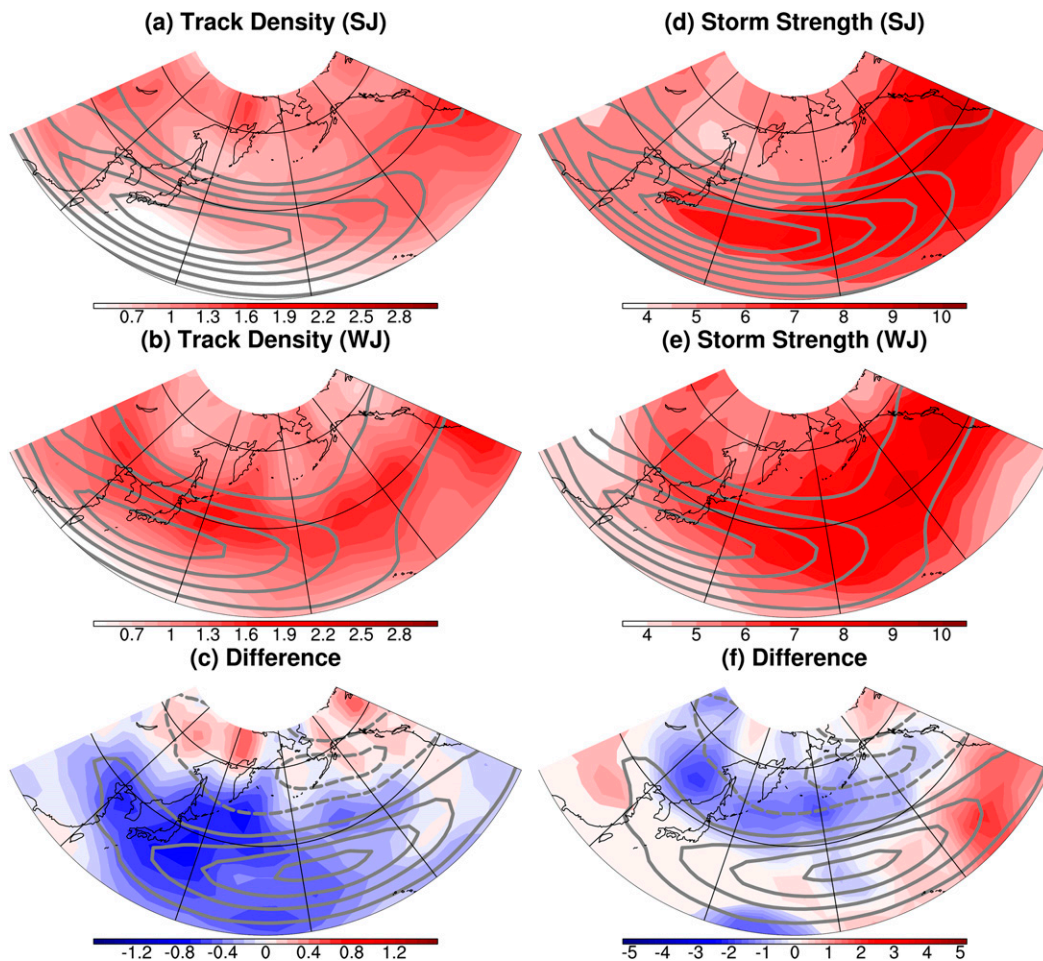
FIG. 6. Distributions of (left) track density (No. per 5° spherical cap) at 300 hPa for (a) the 20 SJ months and (b) the 20 WJ months. (c) The difference between (a) and (b). (d)–(f) As in (a)–(c), respectively, but for storm intensity ($10^{-5}\,\text{s}^{-1}$). The gray contours denote the corresponding 300-hPa zonal wind (m s^{-1}).

and $0.77 \times 10^{-5}\,\text{s}^{-1}$). In contrast, in the northern region $\Gamma_A^{0\rightarrow1}$ is weaker in the strong case ($0.53 \times 10^{14}\,\text{J s}^{-1}$) than in the weak case ($0.71 \times 10^{14}\,\text{J s}^{-1}$), whereas the BCs of both states are similar ($0.68 \times 10^{-5}\,\text{s}^{-1}$ and $0.70 \times 10^{-5}\,\text{s}^{-1}$ for the strong and weak jet states, respectively), implying similar efficiencies for the storms to tap energy from the background fields. In addition, it is found that the southern region (i.e., the jet center) always has larger BC than the northern region, whether in the strong jet state or in the weak jet state. For instance, in the strong jet state, the BCs as a whole in the southern and northern parts are $1 \times 10^{-5}\,\text{s}^{-1}$ and $0.68 \times 10^{-5}\,\text{s}^{-1}$, respectively, implying the storm structure in the jet center may be different from those in the north. The reason for this south–north difference is still unclear. One hypothesis is that the storm systems in the south (i.e., jet center) result from baroclinic instabilities of the jet stream, which can be viewed as modal waves, whereas those in the north are generated through other

mechanisms (e.g., large-scale topographic forcing, diabatic forcing, upper-level short-wave inducing), corresponding to nonmodal waves (Farrell 1984), which are similar to the type-B cyclones described by Petterssen and Smebye (1971). In the atmosphere, evidences show that nonmodal waves dominate (Chung et al. 1976; Chen et al. 1991; Chang 1993; Wang and Rogers 2001; Hoskins and Hodges 2002). This may be the reason why BC peaks in the jet center, but for the TKE, there is less than that in the north.

To see whether the above makes sense, we use a feature-tracking method to do Lagrangian statistics about the storm activity for the two jet states (refer to section 4 for the computation procedure). Figure 6 shows the horizontal distributions of the storm-track density and intensity. It can be seen that in the East Asia–west Pacific region, the track density center is zonally distributed and is located about 10 latitudes north of the jet center (Figs. 6a,b), but the storm intensity maximizes in the jet center (Fig. 6d). Moreover,

the difference in the storm intensity between the two jet states (Fig. 6f) shows a dipolar pattern similar to that of the TKE (Fig. 3f) and that of the zonal wind. All of these characteristics are consistent with the quantitative results in Table 1. That is to say, whether from the viewpoint of a specific jet state or the comparison of the strong and weak jet states, the baroclinic growth rate is generally consistent with the theory of linear baroclinic instability, that is, strong winds entail strong storms. But, because most of the synoptic storms are generated at latitudes far north to the jet core, the large baroclinicity under the strong jet core does not have a significant effect on the storm-track intensity on the whole, though the strong jet locally enhances some of the synoptic storms that migrate near the jet core. One of the reasons why the storm track is weaker in the strong jet state than in the weak jet state is that the baroclinicity in the mid- to high latitudes is too weak in the strong jet state, unfavorable to the storm generation (Fig. 6c) and development (Fig. 6f).

For BT, it is generally consistent with $\Gamma_K^{0 \to 1}$. For instance, its absolute value is greater in the strong jet state than in the weak jet state (Table 1), indicating that the efficiency of the kinetic energy transfer from the storm to the background field is higher in the strong jet. Besides, it is found that the difference in BT between the two jet states is mainly reflected in the central and eastern Pacific (Table 1).

To summarize, $\Gamma_A^{0 \to 1}$ and $\Gamma_K^{0 \to 1}$ together result in weak individual storms in the strong-core jet months. On one hand, in the strong-core jet months, the jet is narrow so that storms in the north are suppressed because of the weak jet wind and reduced baroclinic instability. On the other hand, although the jet wind (and baroclinic instability) in the south is strong, the upscale KE transfer is also strong. These effects collaborate to generate weak storms at the jet core. In addition, $\Gamma_K^{0 \to 1}$ acts to maintain the preexisting jet state, which in turn functions to suppress the storminess in strong-core jets.

Some issues remain. 1) If the upscale KE transfer in the eastern Pacific accounts for the suppression, there should be less TKE in the eastern Pacific in the strong-core jet case than in the weak-core jet case. However, in the southeast corner, TKE is much stronger in the strong-core jet case. The situation there is somehow different. As mentioned above, the zonal wind in the weak-core jet case is too weak over there to support Rossby wave propagation (Randel and Held 1991; Lorenz 2014). 2) The upscale KE transfer is significant only in the central and eastern Pacific, not in the western Pacific (Fig. 5). Then what accounts for the suppression over the southwestern region? This is because, in the energetics balance, there are also nonlocal processes other than canonical transfers that may take effect. As

we will see in the following, the TKE sink induced by $\Gamma_K^{0 \to 1}$ is not necessarily at work locally in the presence of nonlocal processes, such as TKE flux convergence.

c. The nonlocal processes

The nonlocal processes include the convergence of the TAPE, TKE, and geopotential fluxes, representing the processes of energy transport. Figure 7 shows the maps of vertically integrated flux convergence. For the TAPE flux convergence ΔQ_A^1 (Figs. 7a,b), it is positive at the jet core and maximized at the jet exit. On the two flanks of the jet, it is negative, especially on the north flank. This means that the TAPE flux is convergent at the jet core and eastern Pacific, whereas divergent elsewhere. This is the reason why TAPE is concentrated downstream of the jet stream (Figs. 3a,b). The difference in ΔQ_A^1 between the two jet states is shown in Fig. 7c. Both the divergence of the TAPE flux at midlatitudes and in subtropics and the convergence at the jet core and high latitudes are strengthened in the strong-core jet state. For the TKE flux convergence ΔQ_K^1 (Figs. 7d,e), it is negative along the jet stream, whereas positive elsewhere. This means that TKE is generally transported from the western Pacific to the eastern Pacific. The difference in ΔQ_K^1 between the two jet states is shown in Fig. 7f. We see that the convergence (divergence) of the TKE flux is strengthened in the north (south) of the jet core in the strong-core jet state. For the geopotential flux convergence ΔQ_P^1 (Figs. 7g,h), it is negative to the north of the jet core, whereas positive to the south. The difference in ΔQ_P^1 between the two jet states exhibits negative values at the jet core and positive values on its shoulders (Fig. 7i).

From above, we see that strong nonlocal processes exist in the storm-track area, and they differ considerably between the two jet states; this is particularly the case for ΔQ_K^1. In the strong jet state, more TKE is transported downstream (e.g., in the 20°–35°N, 120°–200°E region, the difference in ΔQ_K^1 between the strong and weak jet states is 39% of that of the weak jet state). This is because of the extremely strong transport in the southwest area in the strong jet state, transporting TKE downstream before it is significantly enhanced even in the presence of a strong buoyancy conversion (Fig. 4f). The TKE transported downstream in the strong jet state is finally consumed by $\Gamma_K^{0 \to 1}$. In other words, if there is no strong $\Gamma_K^{0 \to 1}$ in the central and eastern Pacific in the strong jet state, the storm activity over there will be much stronger than that in the weak jet state. That is to say, the TKE sink induced by $\Gamma_K^{0 \to 1}$ is not necessarily revealed locally, when nonlocal processes are in effect. In a word, the storm track as a whole, rather than part of it (e.g., the western Pacific), should be taken in account when studying its dynamics.
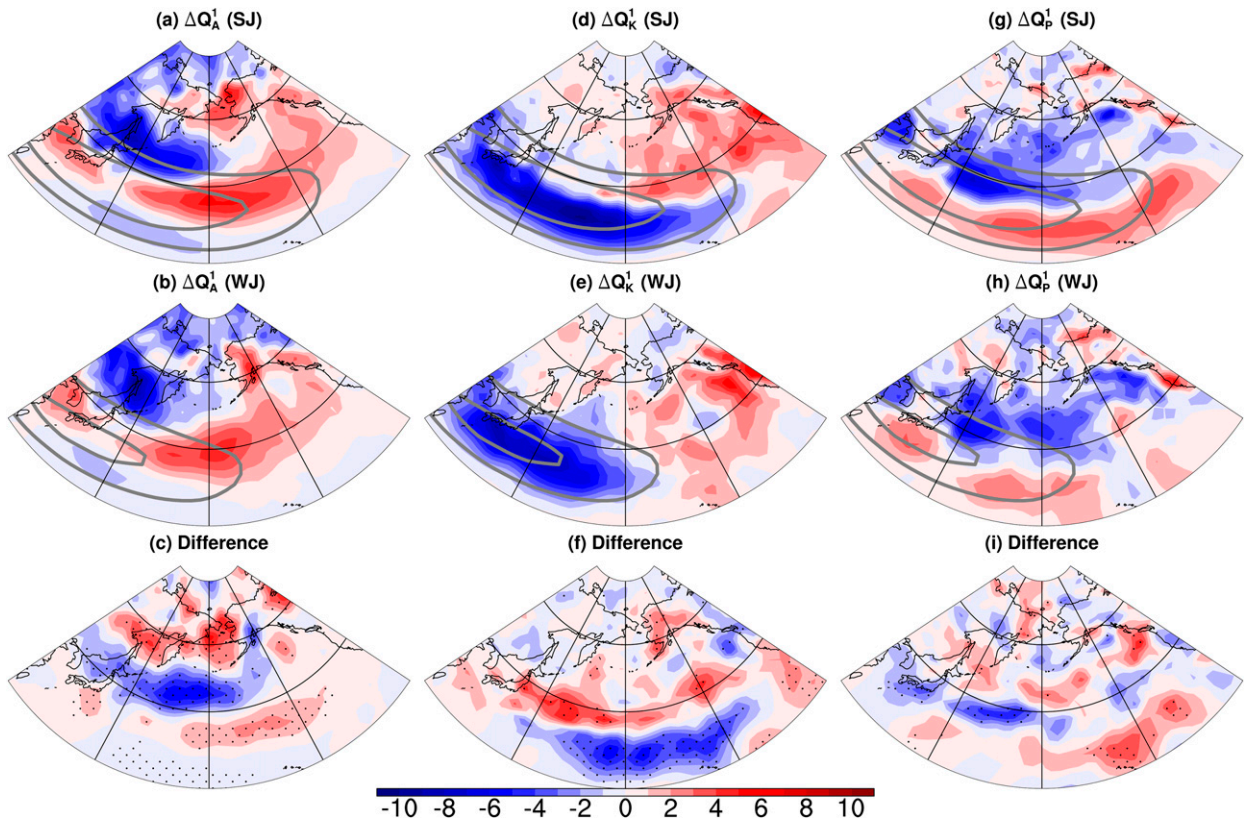
FIG. 7. As in Fig. 5, but for (a)–(c) APE flux convergence, (d)–(f) KE flux convergence, and (g)–(i) geopotential flux convergence. The gray contours show the zonal wind speed of 30 and 50 m s^{-1}.

d. The external forcing

The external forcing mainly comes from diabatic work and frictional dissipation, which are directly related to the increase or decrease of transient eddy energies. Figure 8 shows the maps of vertically integrated diabatic forcing work F_A^1 and frictional dissipation F_K^1 presented by the residues of the APE and KE equations, respectively. We see that F_A^1 is generally positive (Figs. 8a,b). The variable F_A^1 is mainly contributed by latent heating; it acts to increase TAPE. In the strong jet months, F_A^1 is significantly decreased to the east of Japan and over the Sea of Okhotsk (Fig. 8c). Values of F_K^1 are negative over the entire Pacific, especially at the entrance to and in the center of the storm track and along the west coast of North America (Figs. 8d,e). In the strong-core jet months, F_K^1 increases to the east of Japan and along the western coast of North America, whereas it decreases over the central Pacific (Fig. 8f).

e. An energy budget analysis

In this section, we give a quantitative discussion of the Pacific storm-track energetics. Figure 9 gives the energy budgets of the two jet states and their differences in a volume-integrated way. On average, baroclinic transfer and diabatic work are two major TAPE sources. They overall make 80% and 20% of the total TAPE sources, respectively. Buoyancy conversion is the major TAPE sink and is also the only TKE source. Barotropic transfer, together with TKE flux convergence, geopotential flux convergence, and frictional dissipation, damps TKE. Among them, barotropic transfer and frictional dissipation are two major TKE sinks, which make 22% and 51% of the total sinks, respectively. To see how the two jet states are different, we plot in Fig. 9c the difference of these energetics. Generally, only the differences in two terms are significant: diabatic work and barotropic transfer. The diabatic work in the strong jet months is 25% weaker than that in the weak-core jet months, and the upscale KE transfer in the strong jet months is 43% stronger than that in the weak-core jet months. The resultant effect is relatively weak individual storms in the strong-core jet months, consistent with the analysis in the preceding parts. Notice that the baroclinic transfer is overall stronger in the strong-core jet case than in the weak-core jet case, but the difference is not significant. Also notice
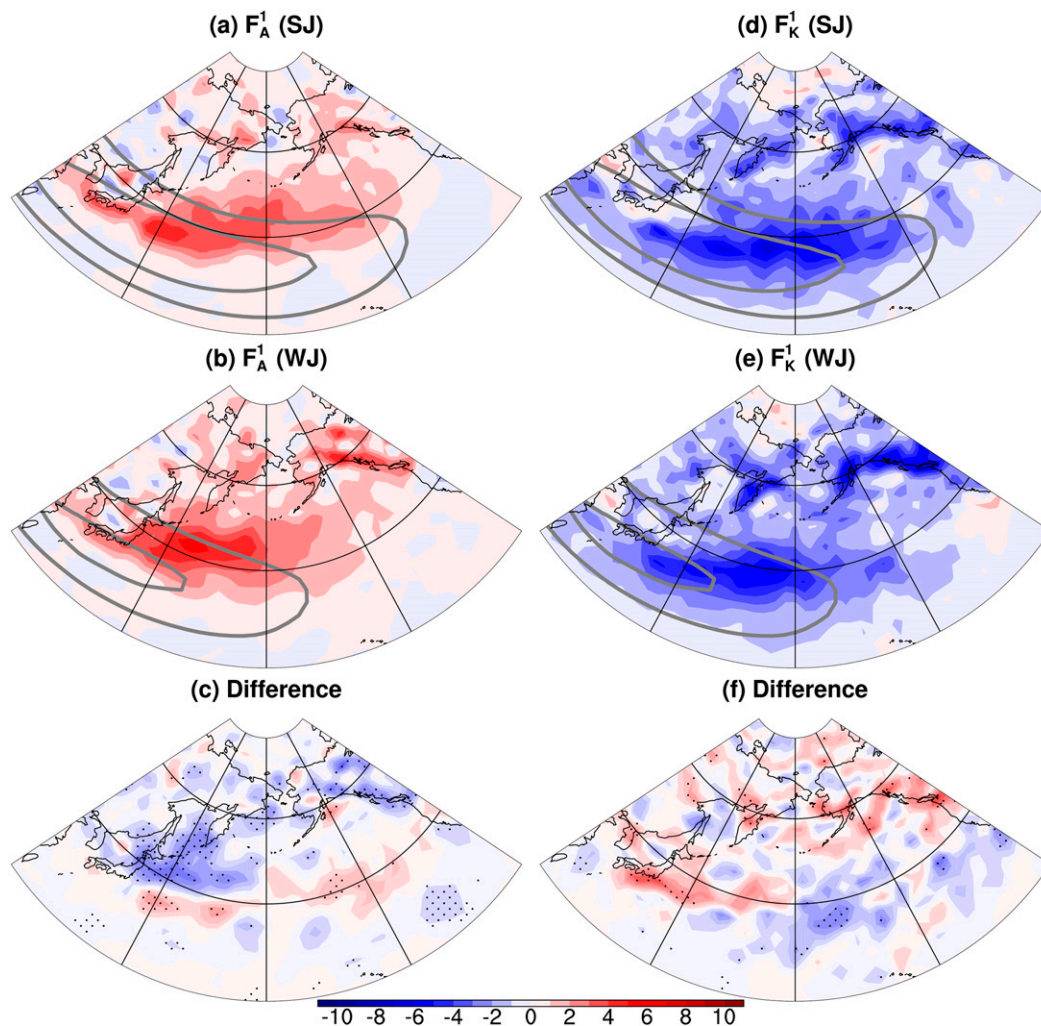
FIG. 8. As in Fig. 7, but for (a)–(c) TAPE generation through diabatic heating and (d)–(f) frictional dissipation.

that, although the baroclinic transfer is overall stronger in the strong-core jet case, its inhomogeneous spatial distribution should be taken into account in explaining the storminess (cf. Fig. 4c and Table 1). The differences in other terms between the two jet states are not significant, either. A detailed budget is summarized in Table 2.

7. The discrepancy in the role of barotropic canonical energy transfer in the variability of the storm-track intensity

So far, there still exists controversy over the role of the barotropic transfer in the formations of the inverse relationship and MWM. For example, Deng and Mak (2005, 2006) and Mak and Deng (2007) argued that the barotropic deformation and the accompanying barotropic energy transfer play an important role in the

storm-track suppression (especially for the MWM), but some other studies (Chang 2001; Harnik and Chang 2004; Chang and Zurita-Gotor 2007) stated that it is not important in either the inverse relationship or the MWM. To further clarify the role of barotropic canonical transfer in these two phenomena, we conduct a quantitative study of this issue from both Eulerian and Lagrangian perspectives.

For the inverse relationship, it has been shown in the preceding part that BT is -0.18×10^{-5} and $-0.11 \times 10^{-5}\,\mathrm{s}^{-1}$ for the strong and weak jet states, respectively. This means that the efficiency of kinetic energy transfer from the perturbation field to the background field is higher in the strong jet state (also true if only the central Pacific and eastern Pacific are considered; refer to Table 1). For MWM, we first select the 20 most significant cases out of the 45 years, according to the suppression index defined by
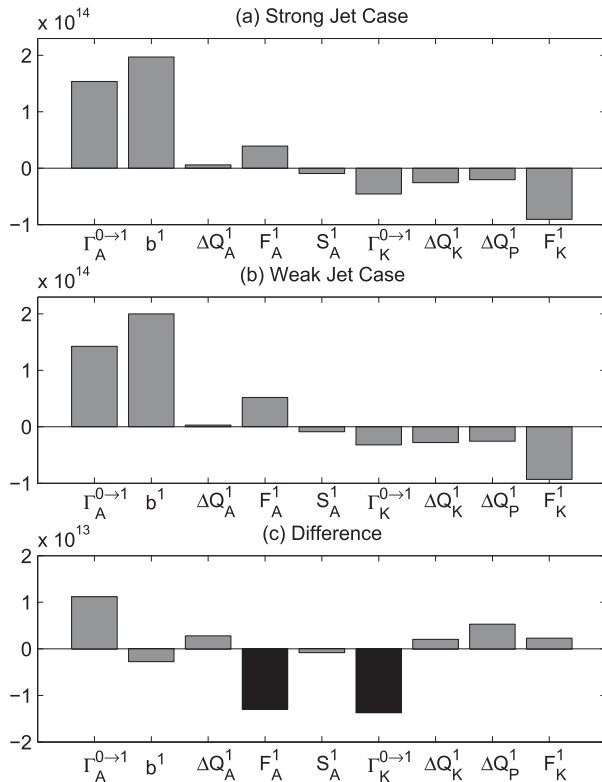
FIG. 9. Energy budgets for (a) the SJ state and (b) the WJ state. (c) The difference between (a) and (b). All quantities have been integrated over the Pacific storm-track area (20°–70°N, 120°–240°E). The bars in black in (c) denote statistical significance at the 0.05 level using the two-sided t test.

$$I_{\mathrm{MWM}} = \mathrm{TKE(Nov)} - \mathrm{TKE(Jan)} - \mathrm{TKE(Feb)}$$
$$+ \mathrm{TKE(Apr)}, \tag{11}$$

where TKE(mo) is the volume-integrated transient kinetic energy of month "mo" in the Pacific storm track (20°–70°N, 120°–240°E; 1000–100 hPa). The following analyses are based on these 20 cases. Figure 10 shows the mean seasonal evolution of the volume-integrated BT in the North Pacific storm-track region. It is obvious that BT has two minima, in November and April, respectively, and a maximum in midwinter, indicating that the efficiency of the upscale KE transfer in early spring

and late autumn is stronger than that in midwinter. That is to say, BT actually functions to cause a maximum storminess in midwinter. But it should be noted that there is a strong downscale KE transfer in the western Pacific (120°E–180°) in winter (the red curve), which may offset the strong upscale KE transfer in the eastern Pacific at the same time. If we analyze only the eastern Pacific region (180°–240°E), we can see that the seasonal evolution of BT (the blue curve) changes, with a relative strengthening in winter and a weakening in spring. Nevertheless, on the whole, the seasonal variation of BT still tends to destroy MWM, rather than generate it. In a word, $\Gamma_K^{0\rightarrow 1}$ works in the opposite direction of MWM. This is consistent with some previous conclusions (Chang 2001; Harnik and Chang 2004; Chang and Zurita-Gotor 2007).

So why does the barotropic canonical transfer play different roles in the inverse relationship and the MWM? First, the barotropic canonical transfer reflects the interaction between the synoptic eddies and the background flow, so its strength depends on both the strength of the eddies and the strength of the jet, and, besides, the configuration between the two (e.g., Vallis and Gerber 2008; Zhang et al. 2012). One can infer that if both the eddy activity and the jet stream are strong, and meanwhile close to each other, then the interaction between them should be strong, and vice versa. Now look at the phenomenon of inverse relationship. Figure 11 shows the distributions of zonal wind, TKE, and the barotropic canonical transfer in the vertical–longitudinal section for both jet states, which have been zonally averaged over the central and eastern Pacific (since the difference in barotropic canonical transfer is most significant there). It can be seen that, in both jet states, the TKE center is located on the northern side of the jet core. Although TKE in the strong jet state (Fig. 11a) is slightly weaker than that in the weak jet state (Fig. 11b), the jet wind and its meridional shear (Fig. 11a) are substantially stronger than those of the weak jet state (Fig. 11b). Therefore, the interaction between the eddies and the background flow is stronger in the strong jet state (Fig. 11a) than in the weak jet state (Fig. 11b), similar to the generalized barotropic governor effect as argued by Deng and Mak (2005).

TABLE 2. Energetics integrated over the Pacific storm-track region (20°–70°N, 120°–240°E) for the two jet states and their differences. The units for TAPE and TKE are 10^{19} J in the top two rows and 10^{18} J in the third row. The remaining columns have units of 10^{14} J s^{-1} in the top two rows and 10^{13} J s^{-1} in the third row. Relative differences are given as percentages. Values in boldface are significant at the 0.05 level using the two-sided t test.

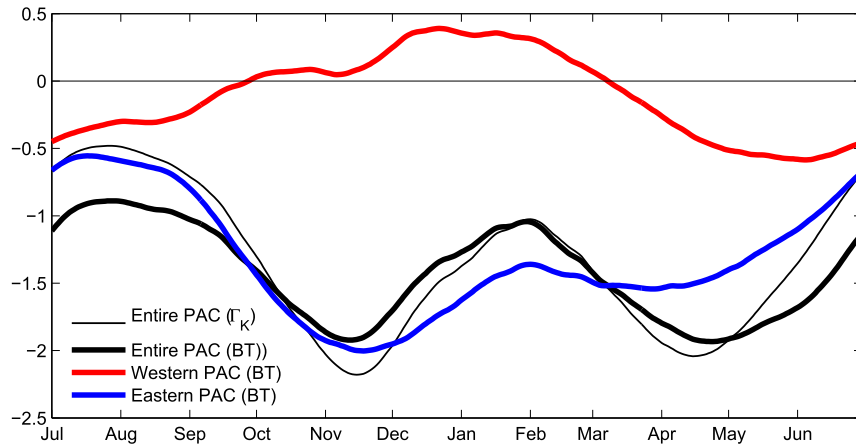|	TAPE	TKE	$\Gamma_A^{0\rightarrow 1}$	F_A^1	S_A^1	b^1	ΔQ_A^1	$\Gamma_K^{0\rightarrow 1}$	ΔQ_K^1	ΔQ_P^1	F_K^1
SJ	1.79	2.55	1.54	0.39	−0.10	1.97	0.06	−0.46	−0.26	−0.20	−0.91
WJ	1.95	2.85	1.43	0.52	−0.09	2.00	0.03	−0.32	−0.28	−0.26	−0.93
Absolute difference (SJ − WJ)	**−1.62**	**−2.92**	1.12	**−1.30**	−0.08	−0.27	0.28	**−1.37**	0.20	0.53	0.23
Relative difference	**[−8.3]**	**[−10.3]**	[7.8]	**[−24.9]**	[9.3]	[−1.4]	[89.0]	**[42.8]**	[−7.3]	[−20.7]	[−2.5]

FIG. 10. Seasonal evolution of volume-integrated $\Gamma_K^{0\rightarrow1}$ (thin black curve; $2.5 \times 10^{13}\,m^2\,s^{-3}$) and BT (thick black curve; $10^{-6}\,s^{-1}$) in the Pacific storm-track domain (20°–70°N, 120°–240°E). The red and blue curves indicate the results of BT ($10^{-6}\,s^{-1}$) in the western Pacific (120°E–180°) and the eastern Pacific (120°–180°E), respectively. Each curve of BT has been normalized by the volume-integrated TKE in the entire Pacific storm-track domain.

Similarly, we take a look at the seasonal variation of the barotropic canonical transfer. Based on above analysis (refer to Fig. 10), we use November to represent the late autumn, and January–February and April to represent the midwinter and early spring, respectively. Figure 12 shows the distributions of the zonal wind,

TKE, and the barotropic canonical transfer in the vertical–longitudinal section of each period, which have been zonally averaged through the central and eastern Pacific. It is obvious that the jet wind is strongest in midwinter (Fig. 12b), followed by autumn (Fig. 12a) and spring (Fig. 12c), but TKE is stronger in spring and
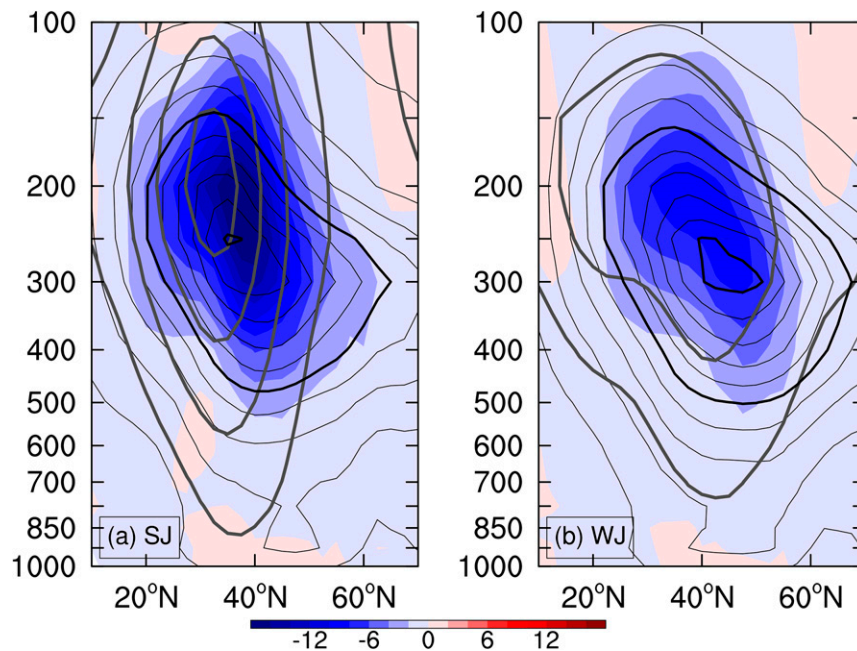
FIG. 11. Vertical–longitudinal distributions of barotropic canonical transfer (shaded; $m^2\,s^{-3}$), TKE (black contours with contour interval of $20\,m^2\,s^{-2}$), and zonal wind (thick gray contours with contour interval of $10\,m\,s^{-1}$) for the (a) strong jet state and (b) weak jet state. All the distributions have been zonally averaged between 180° and 240°E. The thick lines in TKE denote the isolines of 100 and 200 $m^2\,s^{-2}$, respectively.
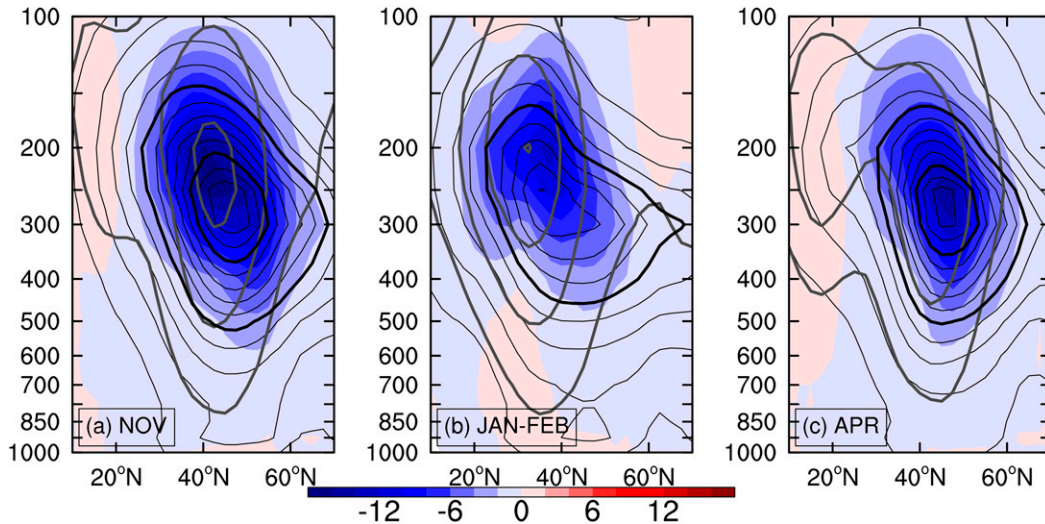
FIG. 12. As in Fig. 11, but for the distributions in (a) November, (b) midwinter (January and February), and (c) April.

autumn than in winter. In addition, it can also be found that although the TKE center is located on the northern side of the jet center during all the three periods, the jet center in midwinter (Fig. 12b) is located more southward and is inclined to the south with height, with the high-level center located at about 30°, which is far from the TKE center (40°N). Therefore, the interaction between the jet stream and midlatitude eddies is inhibited. On the contrary, the jet center and the TKE center are close to each other in autumn (Fig. 12a) and spring (Fig. 12c), favoring the eddy–background flow interaction. This situation is also reflected in the distribution of the barotropic canonical transfer. It can be seen that the $\Gamma_K^{0 \to 1}$ center and the jet center in spring and autumn generally coincide, whereas in midwinter the former is obviously located on the northern side of the later. That is to say, there are two reasons that account for the weaker efficiency of barotropic canonical transfer in midwinter than in spring and fall. One is the weak intensity of the winter storm, and the other is the far distance between the storm and the jet stream in midwinter. These two factors together result in a weak eddy–background flow interaction in midwinter.

The above is also seen in the Lagrangian statistics of the storm activity (the computation is based on the 20 strongest MWM cases). Figure 13 shows the average distributions of track density (counted on each isobaric surface) and storm intensity in the central and eastern Pacific. It can be seen that in spring and autumn the center of the track density (Figs. 13a,c) and the center of the storm intensity (Figs. 13d,f) coincide with the jet center, whereas in winter, first, the track density is low near the jet center (Fig. 13b), and second, the average

storm intensity is weaker than that in spring and autumn, and its center is located on the northern side of the jet center (Fig. 13e). Figure 14 shows the horizontal distribution of 850-hPa track density, overlaid with 300-hPa zonal wind and vertically integrated barotropic canonical transfer. It can be clearly seen that there is an obvious distance between the jet center and the peak location of the storm tracks in midwinter as compared to spring and autumn in agreement with the above observation. As for the peak location of the storm tracks, previous studies (e.g., Brayshaw et al. 2008) indicate that it is likely more closely associated with the midlatitude SST front rather than the tropically driven component of the subtropical jet. We also find there exists a close relation between the SST gradient maximum (in magnitude) and storm-track center (not shown).

In summary, the efficiency of the barotropic canonical transfer (i.e., the interaction) is generally suppressed in midwinter compared to early spring and late fall, but, although the interaction in midwinter is inhibited on the whole, there still exist two situations that should be distinguished: the strong jet state and the weak jet state. They are associated with a relative strong interaction and a relative weak interaction, respectively. More specifically, the interaction depends on three factors: storm intensity, jet strength, and the configuration between the storm and the jet. For the inverse-relationship problem, the relative position of the storm and the jet has little difference between the strong and weak jet states. Although the storms in the strong jet state are weaker than in the weak jet state, the jet wind and its horizontal shear are much stronger than those of the weak jets. Therefore, the eddy–background flow interaction is
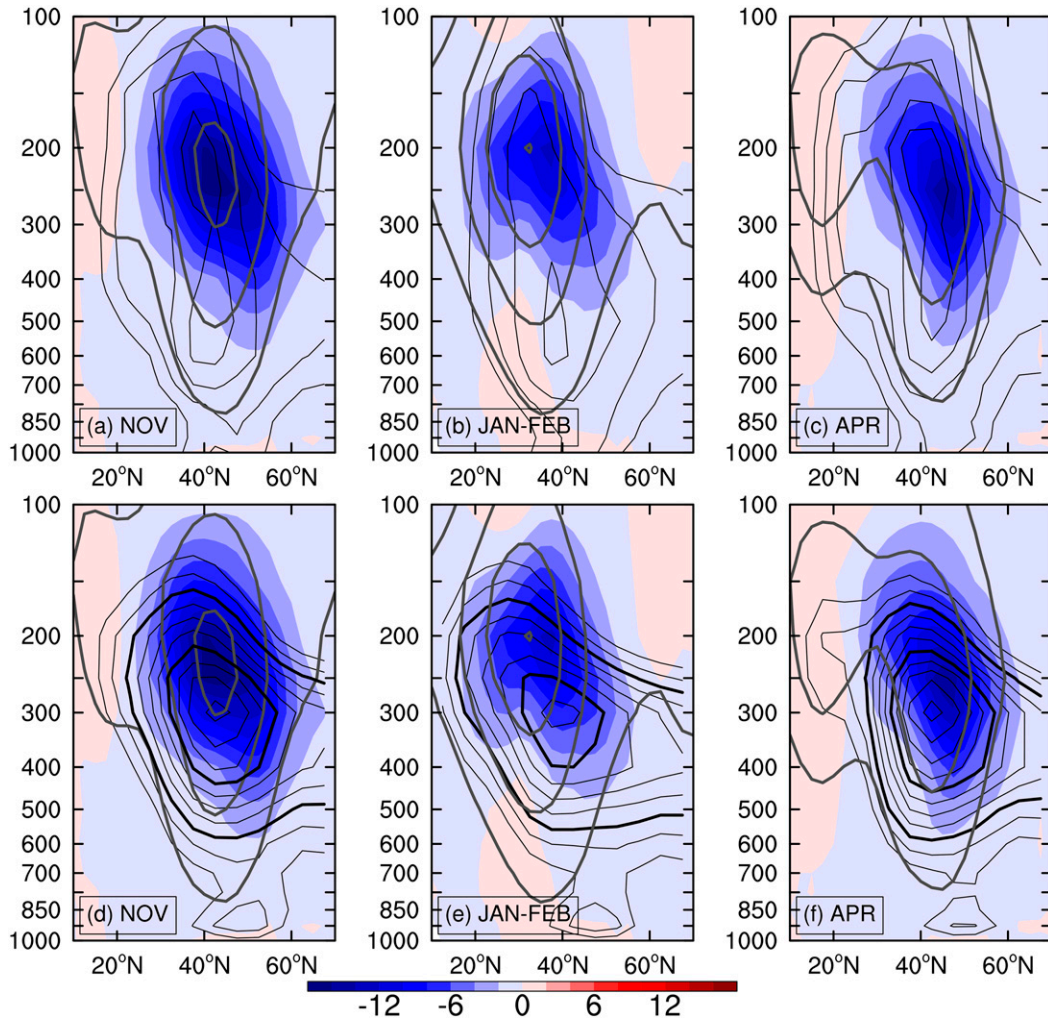
FIG. 13. As in Fig. 12, but for the distributions of (a)–(c) storm-track density [black contours with an interval of 0.2 (30 days)$^{-1}$, starting from 0.8 (30 days)$^{-1}$] and (d)–(f) storm intensity (black contours with an interval of 0.5 × 10^{-5} s^{-1} starting from 4 × 10^{-5} s^{-1}). The thick black lines in storm intensity indicate the isolines of 5 × 10^{-5} and 7 × 10^{-5} s^{-1}, respectively.

stronger in the strong jet case, and the upscale KE transfer, that is, the generalized barotropic governor effect described by Deng and Mak (2005), is also stronger. In contrast, for the seasonal variation problem (i.e., MWM), the jet in winter is located farther southward, far away from the midlatitude synoptic storms. Besides, the occurrence frequency and intensity of the storms in winter are lower and weaker than in spring and autumn. Therefore, the eddy–background flow interaction is weaker in midwinter than in spring and autumn and so is the upscale KE transfer.

8. Conclusions

In boreal winter, the Pacific storm track is unexpectedly weak when the Pacific jet is strong; historically, this counterintuitive phenomenon is called the ''inverse relationship'' between the Pacific storm-track intensity and the jet strength. This study investigates the underlying dynamics of this inverse relationship based on data from ERA-40, using a recently developed methodology, namely, the multiscale window transform (MWT) and the MWT-based theory of canonical transfer and localized multiscale energetics analysis and vorticity analysis (MS-EVA). Just as Penny et al. (2013) found, the linear baroclinic instability theory still holds even in the presence of the overall inverse relationship. Generally, jets with strong (weak) zonal speeds have strong (weak) baroclinic canonical transfers and are hence baroclinically more unstable. But, because most of the synoptic storms are generated at latitudes far north to the jet core, the large baroclinicity under the strong jet
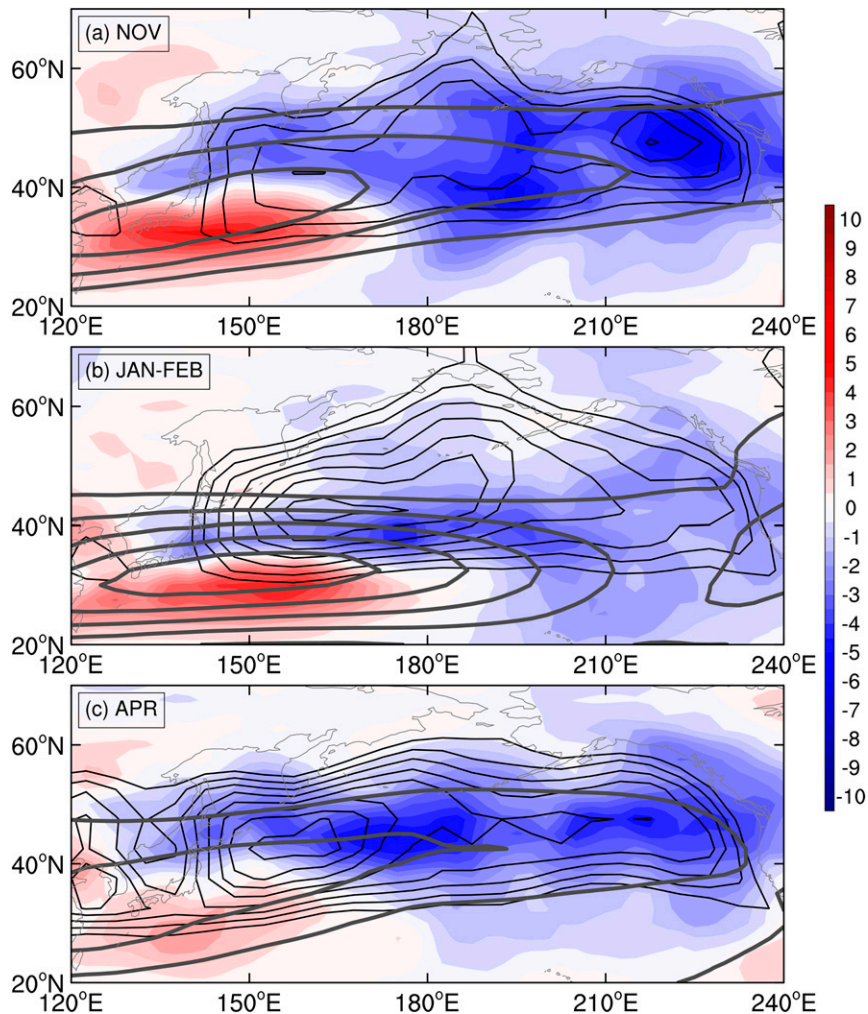
FIG. 14. The horizontal distribution of the storm-track density (thin contours with an interval of 0.1 per 5° spherical cap, starting from 0.8 per 5° spherical cap) at the 850-hPa level. Overlaid is the distribution of vertically integrated barotropic canonical transfer (shaded with an interval of 0.5 $m^2 s^{-3}$) and the 300-hPa zonal wind (thick contours with an interval of 10 $m s^{-1}$ starting from 20 $m s^{-1}$).

core has a low relevance to the storm-track intensity on the whole.

It is found that the inverse relationship is mainly attributed to the internal dynamics in the atmosphere. On one hand, in the strong-core jet state, the jet is so narrow that jet winds in the north are weak, and hence baroclinic instability is greatly reduced there. So in the north, eddies can tap less available potential energy (APE) from the background flow, and then less eddy APE can be converted to eddy kinetic energy (KE), resulting in weak individual storms. On the other hand, although baroclinic instability and buoyancy conversion are strong at the jet core, the upscale canonical KE transfer is even stronger, with more eddy KE transferred back to the background flow. The resultant total (baroclinic plus

barotropic) eddy growth rate is still reduced, and hence the storms in the south are weak, too. Moreover, the inverse KE cascade also acts to maintain the preexisting anomalous jet state and continue to suppress the storms.

Also contributing to the inverse relationship are the diabatic processes. In the strong-core jet months, the eddy APE generation through diabatic processes is significantly weakened, especially at the entrance of the storm track.

In the literature, frequently the inverse relationship is connected to another counterintuitive phenomenon, that is, the midwinter minimum (MWM) of the North Pacific storm track. It is found that the roles that barotropic canonical transfer plays in the generations of the inverse relationship and MWM are actually opposite.

For the former, the jet wind and its horizontal shear with strong jets are much stronger than those with weak jets. Therefore, the eddy–background flow interaction is stronger, and so is the upscale KE transfer, in the strong jet case, just like the generalized barotropic governor effect as described by Deng and Mak (2005). In contrast, for MWM, the jet in winter is located farther southward, far away from midlatitude synoptic storms. In addition, the occurrence frequency and intensity of the storms in winter are lower and weaker than in those spring and autumn. As a result, the eddy–background flow interaction is weaker in midwinter than in spring and autumn, and so is the upscale KE transfer.

In this study, we diagnosed the energetics of the two jet states, that is, the strong jet state and weak jet state. We, however, have not discussed why such two states exist. Based on the above energetics analysis, we see that they may be partially maintained by the transient eddy forcing, consistent with previous studies such as Chang and Guo (2007) and Penny et al. (2013). On the other hand, the Pacific jet state is also influenced by external forcing, for example, tropical convection (Yin 2002; Chang and Guo 2007) and the Asian monsoon (Nakamura et al. 2002). Is the Pacific jet state internally determined or externally driven? Or to what a degree is it driven internally or externally? These questions, among others, which help for a deep understanding of the inverse relationship, will be explored in future studies.

REFERENCES

Anderson, D., K. I. Hodges, and B. J. Hoskins, 2003: Sensitivity of feature-based analysis methods of storm tracks to the form of background field removal. *Mon. Wea. Rev.*, **131**, 565–573, https://doi.org/10.1175/1520-0493(2003)131<0565:SOFBAM>2.0.CO;2.

Blackmon, M. L., 1976: A climatological spectral study of the 500 mb geopotential height of the Northern Hemisphere. *J. Atmos. Sci.*, **33**, 1607–1623, https://doi.org/10.1175/1520-0469(1976)033<1607:ACSSOT>2.0.CO;2.

——, J. M. Wallace, N.-C. Lau, and S. L. Mullen, 1977: An observational study of the Northern Hemisphere wintertime circulation. *J. Atmos. Sci.*, **34**, 1040–1053, https://doi.org/10.1175/1520-0469(1977)034<1040:AOSOTN>2.0.CO;2.

Brayshaw, D. J., B. Hoskins, and M. Blackburn, 2008: The storm-track response to idealized SST perturbations in an aqua-planet GCM. *J. Atmos. Sci.*, **65**, 2842–2860, https://doi.org/10.1175/2008JAS2657.1.

Cai, M., S. Yang, H. M. Van Den Dool, and V. E. Kousky, 2007: Dynamical implications of the orientation of atmospheric eddies: A local energetics perspective. *Tellus*, **59A**, 127–140, https://doi.org/10.1111/j.1600-0870.2006.00213.x.

Chang, E. K. M., 1993: Downstream development of baroclinic waves as inferred from regression analysis. *J. Atmos. Sci.*, **50**, 2038–2053, https://doi.org/10.1175/1520-0469(1993)050<2038:DDOBWA>2.0.CO;2.

——, 2001: GCM and observational diagnoses of the seasonal and interannual variations of the Pacific storm track during the cool season. *J. Atmos. Sci.*, **58**, 1784–1800, https://doi.org/10.1175/1520-0469(2001)058<1784:GAODOT>2.0.CO;2.

——, 2003: Midwinter suppression of the Pacific storm track activity as seen in aircraft observations. *J. Atmos. Sci.*, **60**, 1345–1358, https://doi.org/10.1175/1520-0469(2003)60<1345:MSOTPS>2.0.CO;2.

——, and I. Orlanski, 1993: On the dynamics of a storm track. *J. Atmos. Sci.*, **50**, 999–1015, https://doi.org/10.1175/1520-0469(1993)050<0999:OTDOAS>2.0.CO;2.

——, and Y. Guo, 2007: Dynamics of the stationary anomalies associated with the interannual variability of the midwinter Pacific storm track—The roles of tropical heating and remote eddy forcing. *J. Atmos. Sci.*, **64**, 2442–2461, https://doi.org/10.1175/JAS3986.1.

——, and P. Zurita-Gotor, 2007: Simulating the seasonal cycle of the Northern Hemisphere storm tracks using idealized non-linear storm-track models. *J. Atmos. Sci.*, **64**, 2309–2331, https://doi.org/10.1175/JAS3957.1.

——, S. Lee, and K. L. Swanson, 2002: Storm track dynamics. *J. Climate*, **15**, 2163–2183, https://doi.org/10.1175/1520-0442(2002)015<02163:STD>2.0.CO;2.

Chen, S.-J., Y.-H. Kuo, P.-Z. Zhang, and Q.-F. Bai, 1991: Synoptic climatology of cyclogenesis over East Asia, 1958–1987. *Mon. Wea. Rev.*, **119**, 1407–1418, https://doi.org/10.1175/1520-0493(1991)119<1407:SCOCOE>2.0.CO;2.

Christoph, M., U. Ulbrich, and P. Speth, 1997: Midwinter suppression of Northern Hemisphere storm track activity in the real atmosphere and in GCM experiments. *J. Atmos. Sci.*, **54**, 1589–1599, https://doi.org/10.1175/1520-0469(1997)054<1589:MSONHS>2.0.CO;2.

Chung, Y.-S., K. D. Hage, and E. R. Reinelt, 1976: On lee cyclogenesis and airflow in the Canadian Rocky Mountains and the East Asian Mountains. *Mon. Wea. Rev.*, **104**, 879–891, https://doi.org/10.1175/1520-0493(1976)104<0879:OLCAAI>2.0.CO;2.

Deng, Y., and M. Mak, 2005: An idealized model study relevant to the dynamics of the midwinter minimum of the Pacific storm track. *J. Atmos. Sci.*, **62**, 1209–1225, https://doi.org/10.1175/JAS3400.1.

——, and ——, 2006: Nature of the differences in the intraseasonal variability of the Pacific and Atlantic storm tracks: A diagnostic study. *J. Atmos. Sci.*, **63**, 2602–2615, https://doi.org/10.1175/JAS3749.1.

Eady, E. T., 1949: Long waves and cyclone waves. *Tellus*, **1A** (3), 33–52, https://doi.org/10.3402/tellusa.v1i3.8507.

Farrell, B., 1984: Modal and non-modal baroclinic waves. *J. Atmos. Sci.*, **41**, 668–673, https://doi.org/10.1175/1520-0469(1984)041<0668:MANMBW>2.0.CO;2.

Harnik, N., and E. K. M. Chang, 2004: The effects of variations in jet width on the growth of baroclinic waves: Implications for midwinter Pacific storm track variability. *J. Atmos. Sci.*, **61**, 23–40, https://doi.org/10.1175/1520-0469(2004)061<0023:TEOVIJ>2.0.CO;2.

Hodges, K. I., 1995: Feature tracking on the unit sphere. *Mon. Wea. Rev.*, **123**, 3458–3465, https://doi.org/10.1175/1520-0493(1995)123<3458:FTOTUS>2.0.CO;2.

Hoskins, B. J., and K. I. Hodges, 2002: New perspectives on the Northern Hemisphere winter storm tracks. *J. Atmos. Sci.*, **59**, 1041–1061, https://doi.org/10.1175/1520-0469(2002)059<1041:NPOTNH>2.0.CO;2.

Ioannou, P., and R. S. Lindzen, 1986: Baroclinic instability in the presence of barotropic jets. *J. Atmos. Sci.*, **43**, 2999–3014, https://doi.org/10.1175/1520-0469(1986)043<2999:BIITPO>2.0.CO;2.

James, I. N., 1987: Suppression of baroclinic instability in horizontally sheared flows. *J. Atmos. Sci.*, **44**, 3710–3720, https://doi.org/10.1175/1520-0469(1987)044<3710:SOBIIH>2.0.CO;2.

Lee, S.-S., J.-Y. Lee, B. Wang, F.-F. Jin, W.-J. Lee, and K.-J. Ha, 2011: A comparison of climatological subseasonal variations in the wintertime storm track activity between the North Pacific and Atlantic: Local energetics and moisture effect. *Climate Dyn.*, **37**, 2455–2469, https://doi.org/10.1007/s00382-011-1027-z.

Liang, X. S., 2016: Canonical transfer and multiscale energetics for primitive and quasigeostrophic atmospheres. *J. Atmos. Sci.*, **73**, 4439–4468, https://doi.org/10.1175/JAS-D-16-0131.1.

——, and A. R. Robinson, 2005: Localized multiscale energy and vorticity analysis. *Dyn. Atmos. Oceans*, **38**, 195–230, https://doi.org/10.1016/j.dynatmoce.2004.12.004.

——, and D. G. M. Anderson, 2007: Multiscale window transform. *Multiscale Model. Simul.*, **6**, 437–467, https://doi.org/10.1137/06066895X.

——, and A. R. Robinson, 2007: Localized multi-scale energy and vorticity analysis: II. Finite-amplitude instability theory and validation. *Dyn. Atmos. Oceans*, **44**, 51–76, https://doi.org/10.1016/j.dynatmoce.2007.04.001.

Lindzen, R. S., and B. Farrell, 1980: A simple approximate result for the maximum growth rate of baroclinic instabilities. *J. Atmos. Sci.*, **37**, 1648–1654, https://doi.org/10.1175/1520-0469(1980)037<1648:ASARFT>2.0.CO;2.

Lorenz, D. J., 2014: Understanding midlatitude jet variability and change using Rossby wave chromatography: Wave–mean flow interaction. *J. Atmos. Sci.*, **71**, 3684–3705, https://doi.org/10.1175/JAS-D-13-0201.1.

Lorenz, E. N., 1955: Available potential energy and the maintenance of the general circulation. *Tellus*, **7**, 157–167, https://doi.org/10.3402/tellusa.v7i2.8796.

Mak, M., and Y. Deng, 2007: Diagnostic and dynamical analyses of two outstanding aspects of storm tracks. *Dyn. Atmos. Oceans*, **43**, 80–99, https://doi.org/10.1016/j.dynatmoce.2006.06.004.

Nakamura, H., 1992: Midwinter suppression of baroclinic wave activity in the Pacific. *J. Atmos. Sci.*, **49**, 1629–1642, https://doi.org/10.1175/1520-0469(1992)049<1629:MSOBWA>2.0.CO;2.

——, and T. Sampe, 2002: Trapping of synoptic-scale disturbances into the North-Pacific subtropical jet core in midwinter. *Geophys. Res. Lett.*, **29**, 1761, https://doi.org/10.1029/2002GL015535.

——, T. Izumi, and T. Sampe, 2002: Interannual and decadal modulations recently observed in the Pacific storm track activity and East Asian winter monsoon. *J. Climate*, **15**, 1855–1874, https://doi.org/10.1175/1520-0442(2002)015<1855:IADMRO>2.0.CO;2.

Orlanski, I., and J. Katzfey, 1991: The life cycle of a cyclone wave in the Southern Hemisphere. Part I: Eddy energy budget. *J. Atmos. Sci.*, **48**, 1972–1998, https://doi.org/10.1175/1520-0469(1991)048<1972:TLCOAC>2.0.CO;2.

Penny, S., G. H. Roe, and D. S. Battisti, 2010: The source of the midwinter suppression in storminess over the North Pacific. *J. Climate*, **23**, 634–648, https://doi.org/10.1175/2009JCLI2904.1.

——, D. S. Battisti, and G. H. Roe, 2013: Examining mechanisms of variability within the Pacific storm track: Upstream seeding and jet-core strength. *J. Climate*, **26**, 5242–5259, https://doi.org/10.1175/JCLI-D-12-00017.1.

Petterssen, S., and S. J. Smebye, 1971: On the development of extratropical cyclones. *Quart. J. Roy. Meteor. Soc.*, **97**, 457–482, https://doi.org/10.1002/qj.49709741407.

Plumb, R. A., 1983: A new look at the energy cycle. *J. Atmos. Sci.*, **40**, 1669–1688, https://doi.org/10.1175/1520-0469(1983)040<1669:ANLATE>2.0.CO;2.

Randel, W. J., and I. M. Held, 1991: Phase speed spectra of transient eddy fluxes and critical layer absorption. *J. Atmos. Sci.*, **48**, 688–697, https://doi.org/10.1175/1520-0469(1991)048<0688:PSSOTE>2.0.CO;2.

Swanson, K., 2007: Storm track dynamics. *The Global Circulation of the Atmosphere*, T. Schneider and A. H. Sobel, Eds., Princeton University Press, 78–103.

Uppala, S. M., and Coauthors, 2005: The ERA-40 Re-Analysis. *Quart. J. Roy. Meteor. Soc.*, **131**, 2961–3012, https://doi.org/10.1256/qj.04.176.

Vallis, G. K., and E. P. Gerber, 2008: Local and hemispheric dynamics of the North Atlantic Oscillation, annular patterns and the zonal index. *Dyn. Atmos. Oceans*, **44**, 184–212, https://doi.org/10.1016/j.dynatmoce.2007.04.003.

Wang, C.-C., and J. C. Rogers, 2001: A composite study of explosive cyclogenesis in different sectors of the North Atlantic. Part I: Cyclone structure and evolution. *Mon. Wea. Rev.*, **129**, 1481–1499, https://doi.org/10.1175/1520-0493(2001)129<1481:ACSOEC>2.0.CO;2.

Wilks, D. S., 2011: *Statistical Methods in the Atmospheric Sciences*. 3rd ed. Academic Press, 676 pp.

Yin, J. H., 2002: *The Peculiar Behavior of Baroclinic Waves during the Midwinter Suppression of the Pacific Storm Track*. University of Washington, 137 pp.

Zhang, Y., X.-Q. Yang, Y. Nie, and G. Chen, 2012: Annular mode–like variation in a multilayer quasigeostrophic model. *J. Atmos. Sci.*, **69**, 2940–2958, https://doi.org/10.1175/JAS-D-11-0214.1.

Zhang, Y., and I. M. Held, 1999: A linear stochastic model of a GCM's midlatitude storm tracks. *J. Atmos. Sci.*, **56**, 3416–3435, https://doi.org/10.1175/1520-0469(1999)056<3416:ALSMOA>2.0.CO;2.